Supplemental Online Information

Supplemental Methods

Mouse models

All animal procedures were reviewed by the Institutional Animal Care and Use Committee and approved by veterinarian state authority (LAVES) in compliance with the humane care and use of laboratory animals. Unless indicated otherwise, we used male mice aged 12-16 weeks back-crossed for at least 10 generations in the C57BL/6N background. The generation of the RyR2-S2808A$^{+/+}$ and RyR2-S2814A$^{+/+}$ knock-in mouse strains was described previously (1-3). For genotyping we used the following primer pairs: RyR2-S2808A, F 5'-ATCCCGAGGTAATCAGGTTTCT-3', R 5'-AGTTGGGTTCAAAGTTCTAGGC-3'; and digested the PCR product by Fsp I restriction enzyme (New England Biolabs). RyR2-S2814A, F 5'-GCCTTGTGTTTCTGAAGGCTCTTACTGC-3', R 5'-CTACAGGACGTAGGAAGGATGGAACC-3', and subsequent Cla I restriction enzyme (New England Biolabs) digest of the PCR product. PLN$^{-/-}$ knock-out mice were described previously (4). Titin-eGFP knock-in mice were backcrossed into the 129/S6 background as described previously (5). Epac1-camps transgenic mice expressed a cAMP-specific ubiquitous FRET-biosensor as described previously (6).

Cardiac myocyte isolation from mouse hearts

For isolation of atrial (AM) and ventricular (VM) myocytes, mice were euthanized, hearts rapidly extracted, and the aorta connected to a 21-G cannula. Using a modified Langendorff setup the heart was perfused with nominally Ca^{2+} free oxygenated

perfusion buffer (Supplemental Table 4) for 4 min at 37 °C and a flow rate of 4 mL/min. Next, the perfusate was switched to collagenase type II containing perfusion buffer for further 8 min (600 U/mL, Worthington Biochemical Corporation). Following digestion, atrial versus ventricular tissues were separately harvested using microsurgical scissors (Fine Science Tools GmbH, 15025-10), gently minced in collagenase-containing buffer, and triturated by a 5 mL Pasteur pipette to suspend the myocytes in solution. Residual tissue fragments were cleared through a 100 µm cell strainer (BD Falcon, 352360). Collagenase activity was stopped in perfusion buffer by 10% (v/v) bovine calf serum (HyClone Laboratories). Isolated myocytes were washed three times via 8 min gravity sedimentation and re-suspension before plating on laminin (mouse laminin, BD Biosciences) coated glass coverslips (Ø 18 mm, Thermo Scientific) for 15 min prior to immunofluorescence staining. Laminin coating was not used for sarcomere shortening measurements. For physiological Ca^{2+} imaging and sarcomere shortening measurements, the Ca^{2+} concentration was gradually increased to 1 mM. For analysis of cell size and morphological cell quality, AM and VM were individually documented by transmitted light imaging (Zeiss LSM 710, Jena, Germany) and cell dimensions were determined with Fiji (http://fiji.sc/). Additional details about the analysis have been described previously (7).

Indirect immunofluorescence microscopy (IF)

Following plating on laminin-coated coverslips, AM or VM were fixed in 4% (w/v) paraformaldehyde for 5 min followed by three PBS washing steps (pH 7.4, $CaCl_2$ and $MgCl_2$ free, GIBCO). Next, cells were incubated overnight in blocking/permeabilization buffer (10% v/v bovine calf serum, 0.2% v/v Triton in PBS). The primary antibodies were

diluted in blocking buffer and incubated overnight at 4 °C. Please refer to Supplemental Table 3 for detailed information regarding all primary antibodies. Subsequently, myocytes were washed three times in blocking buffer and incubated with Alexa Fluor 514 and 633 secondary antibodies (A-31555, A-21071, lifetechnologies) for 2 h at room temperature. Co-immunofluorescence staining by combined mouse or rabbit antibodies (Cav3 + RyR2; JP2 + pS2808) required direct labeling of the primary antibodies with Zenon Alexa Fluor 555 and 647 mouse IgG labeling reagent as per the manufacturer's instructions (Z25008 and Z25308, lifetechnologies). Following antibody incubation, cardiomyocytes were washed three times in PBS and embedded in mounting medium (ProLong Gold Antifade Reagent, lifetechnologies).

Supplemental Figure 6 shows confocal IF experiments using custom-made peptides specific for the de-phosphorylated versus phosphorylated RyR2-S2808 site with the following respective aa. sequences: H_2N-CRT RRI SQT SQV-$CONH_2$; H_2N-CRT RRI S(PO_3H_2)QT SQV-$CONH_2$ (Eurogentec). These peptides were used to establish the RyR2-pS2808 epitope-specific antibody signals of RyR2 clusters in situ as reported. For this, the primary antibody specific for the protein kinase A (PKA) phosphorylated RyR2-pS2808 site described previously (1, 2) was incubated with each peptide in blocking buffer 20 min prior to application.

RyR2-pS2808 and -pS2814 signal analysis of RyR2-clusters

Normalized pS2808- and pS2814-signals were calculated from confocal immunofluorescence images of 100 x 100 nm pixel size. ROIs were used to define individual cells as shown in Supplemental Figure 5A. Nuclear signals of the RyR2-pS2808 and RyR2-pS2814 antibodies (Badrilla Ltd.) reflect unspecific cross-reactions

(please refer to Figure 3A/D and Supplemental Table 3) and were omitted from the signal analysis. Cytosolic RyR2-pS2808, RyR2-pS2814 and RyR2 signals were background-corrected by subtracting the modal grayscale value for each ROI. RyR2-clusters were identified after local contrast enhancement and image smoothing (3x3 mean filter) as contiguous signal areas around local signal maxima within a maximum tolerance of 15 grayscale levels (8-bit). A binarized image representing the combined cluster detection from both channels was generated, dilated, and subjected to water shedding. For each resulting cluster-segment the average normalized RyR2-pS2808 or RyR2-pS2814 signal was calculated as pS2808/RyR2 or pS2814/RyR2 ratio data, respectively. The distribution of all RyR2-pS2808 and RyR2-pS2814 signals throughout a given cluster population was graphed as histogram (bin size 0.2). Paired experimental data (i.e., AM versus VM or control versus ISO) were normalized to the position of the first peak in the control population. For the sham versus post-TAC data from AM cells, we determined the highly PKA-phosphorylated (highphos) RyR2 clusters by using the 2^{nd} peak position of the cluster phosphorylation distribution in the control population as threshold. This approach determined the fraction of highly phosphorylated RyR2-clusters among all clusters as presented in Figure 8E.

Proximity analysis of RyR2-pS2808 or RyR2-pS2814 signals and Cav3-clusters

In analogy to the RyR2-pS2808 or RyR2-pS2814 signal and RyR2-cluster analysis described above, the spatial relations between caveolin-3 (Cav3) clusters were calculated from confocal immunofluorescence images of 100 nm pixel size. The Cav3 signals were binarized by local Otsu-thresholding (radius 1 µm) following local contrast enhancement and image smoothing (3x3 mean filter). In parallel, after background

correction and image filtering (3x3 mean filter) the local positions of typical punctate RyR2-pS2808 or RyR2-pS2814 signals apparent as in situ phosphorylated clusters were determined as local signal maxima (at 5 grayscale levels noise tolerance). Consequently, pS2808 and pS2814 signal intensities were measured at local signal maxima positions and normalized to the 90^{th} percentile for each cell (pS2808: n=7; pS2814: n=20). Signal intensities showed a Gaussian distribution with a mean intensity of 0.68±0.07 for pS2808 signals and 0.65±0.3 for pS2814 signals, respectively (S.D.; a.u.). For pS2808 and pS2814 signals two types of RyR2-clusters were identified, respectively: lowphos clusters for intensities smaller than the average signal and highphos clusters for intensities above the average signal; segmentation outputs were visualized and presented exemplarily in Figures 3C and 3F.

Furthermore, the correlation between the RyR2-pS2808 or RyR2-pS2814 signal intensity and the spacing of RyR2- and Cav3-clusters was investigated (Supplemental Figure 8). For this, the NND of central RyR2-clusters to Cav3-clusters was calculated within ROIs that exclude the surface-bound sarcolemmal membrane and the nucleus. The RyR2-Cav3 NNDs were related to the RyR2-pS2808 and -pS2814 signal intensity of corresponding RyR2-clusters, respectively. Average NND values were calculated for a) consecutive bins (0.1 width) of the normalized RyR2-pS2808 and RyR2-pS2814 intensities (Supplemental Figures 8A and 8C) and b) for lowphos versus highphos RyR2-clusters (Supplemental Figure 8B and 8D). Statistical testing was performed by Mann-Whitney as indicated.

TAT network analysis

Two-dimensional skeleton images were extracted from confocal live cell images of TAT membrane networks stained with di-8-ANEPPS in AM and VM using Fiji as described (7, 8). For individual cells, ROIs were selected excluding the surface sarcolemmal membrane. Following background subtraction and smoothing, a statistical region-merging algorithm was applied (8). ROIs were converted into binary images using a predefined threshold and skeletonized using the plugin "*Skeletonize (2D/3D)*". The total skeleton length and the number of branching points were automatically analyzed using the plugin "*Analyze Skeleton (2D/3D)*" (9). Orientations of individual TAT network components were analyzed with the Fiji plugin "Directionality" (10) computing a histogram for each image, which indicated the frequency of any individual TAT component orientation for a given direction using 1° as bin size. Histogram data from groups of cells were averaged and TAT components with a specific orientation presented relative to the axial (a.k.a. longitudinal) cell axis. By definition AT components correspond to the 0° and TT components to the 90° bin as described previously (7, 11). Automated commands are documented below.

Skeleton

```
run("Subtract Background...", "rolling=5");
run("Enhance Local Contrast (CLAHE)", "blocksize=49 histogram=256 maximum=3 mask=*None*");
run("Smooth");
run("Statistical Region Merging", "q=100 showaverages");
run("8-bit");
```

```
setThreshold(25, 255);
run("Convert to Mask");
run("Skeletonize (2D/3D)");
run("Analyze Skeleton (2D/3D)", "prune=none");
```

Directionality

```
run("Directionality", "method=[Fourier components] nbins=180 histogram=-45 display_table");
```

Live cell STED super-resolution microscopy and data analysis

For super-resolution imaging of select TAT membrane components a custom STimulated Emission Depletion (STED) setup and user-defined algorithms were used as described previously (11). Excitation of di-8-ANEPPS and de-excitation by the STED beam was performed with synchronized pulsed lasers. For excitation, a pulsed 490 nm diode laser used 3 µW for confocal and 10 µW for STED images. De-excitation occurred at 750 nm (200 mW) by a Ti:Sapphire laser (80 MHz; Coherent). Laser beams were focused through a 100x 1.4 NA oil objective, fluorescence filtered by a 675±30 nm bandpass, and detected by an avalanche photodiode. Images were recorded by resonant mirror (x-direction, 15,8 kHz) and piezo stage scanning (y-direction). A pixel size of 20 nm x 20 nm and a pixel dwell time of 20 µs were used. All STED images were linearly deconvolved (Wiener filter) using a two-dimensional Lorentz function (Kernel 50 nm; MATLAB R2009b).

To determine the dimension of optical cross-sections for example for TT components, a 2D Gauss function was fitted to the fluorescence signal of individual TTs of STED

images using MATLAB (R2009b). The orientation of the axis fit was aligned with the main axial cell axis (X) and its perpendicular transversal axis (Y) as previously described (11). The full width at half maximum of each fitted section was determined and represented as average width δ for n optical sections. All measured and calculated data are summarized in Figure 1C and Supplemental Table 1.

High-pressure freezing and electron tomography

For high-pressure freezing, pelleted isolated AM were placed in 200 µm aluminium type A specimen carriers coupled with type B lids and the specimens were rapidly frozen with a HPM100 (Leica). Freeze substitution was performed for 24 h in 1% OsO_4 in acetone using an AFS2 (Leica). Specimens were dehydrated in graded acetone, and embedded in Epon-Araldite resin. Semi-thick (280 nm) sections were placed on formvar-coated slot-grids, post stained with 2% aqueous uranyl acetate and Reynold's lead citrate. Colloidal gold particles (15 nm) were added to both surfaces of the sections to serve as fiducial markers for tilt series alignment. Preparations were imaged at the EMBL Heidelberg Electron microscopy core facility and at the Boulder Laboratory for 3D Electron Microscopy of Cells (University of Colorado, Boulder, CO) using an intermediate voltage electron microscope (Tecnai TF30; FEI, Eindhoven, The Netherlands) operating at 300 kV. Images were captured on a 4K x 4K charge-coupled device camera (UltraScan; Gatan, Pleasanton, CA) using the SerialEM software package. For imaging, the specimen holder was tilted from +60° to -60° at 1° intervals. For dual-axis tilt series the specimen was then rotated by 90° in the X-Y plane, and another +60° to -60° tilt series was taken. The images from each tilt-series were aligned by fiducial marker tracking and back-projected to generate two single full-thickness

reconstructed volumes (tomograms), which were then combined to generate a single high-resolution 3D reconstruction of the original partial cell volume (12). Isotropic voxel size ranged from 0.765-1.206 nm. In some instances, tomograms were computed from montaged stacks, to increase the total reconstructed tissue to up to 10 µm x 10 µm in X-Y. Biologically meaningful resolution was approximately 4 nm in X-Y. All tomograms were processed and analysed using IMOD software (13), which was also used to generate 3D models of relevant structures of interest (14). Models were smoothed and meshed to obtain the final 3D representation, in which spatial relations of various cardiomyocyte sub-structures were quantified. For visualisation of AT-SR junction, a traffic light system was implemented, where rendering in red depicted AT–SR junctions ≤15nm in gap width containing RyR2 densities, yellow, AT–SR junctions ≤20nm in gap width but lacking RyR2 densities, and green, membrane areas with no apparent junctions (Supplemental Figure 4).

Nearest-neighbour-distance analysis of RyR2-clusters

Fixed and permeabilized AM or VM were incubated with the RyR2 primary antibody (MA3-916; Supplemental Table 3) overnight at 4°C, and the anti-mouse secondary antibody labeled with the dye KK114 (15) for 2 h at room temperature. The same blocking, washing and mounting described for confocal IF images were used. STED imaging used a custom setup described previously (11). KK114 excitation occured at 635 nm (Diode LDH-P-635, PicoQuant, Berlin, Germany) and STED depletion at 750 nm. Emitted fluorescence was bandpass filtered at 675±30 nm. STED imaging was performed with a pinhole of 100 µm, a dwell time of 150 µs, and a 20 nm step-size.

For analysis, we identified regions of high local RyR2 density using the local signal maxima in STED images within a tolerance interval of 15 grayscale levels (8-bit) after 5 x 5 median filter smoothing. The spacing between adjacent signal maxima was analyzed by nearest-neighbour-distance (NND). NND distributions were calculated with 40 nm bin size for AM or VM. The presented data include 19 AM (2793 local peaks) and 18 VM (3102 local peaks) from 2 mouse hearts. For comparison of AM versus VM, the likelihood of a peak to have a nearest neighbour within 200–440 nm distance was confirmed by Student's t-test.

Cav1.2 signal analysis

Fixed and permeabilized AM were incubated with Cav1.2 (ACC-003) and Cav3 primary antibodies (Supplemental Table 3) overnight at 4°C, and secondary antibodies anti-rabbit Abberior STAR 580 and anti-mouse Abberior STAR 488 (2-0012-005-8, 2-0002-006-8; Abberior GmbH) for 2 h at room temperature. The same blocking, washing and mounting as described for confocal IF images were used. For imaging a Leica TCS SP8 STED super-resolution microscope was used at a resolution approximating 50 nm.

For analysis, Cav1.2 clusters were extracted from STED images within intracellular regions of interests omitting the sarcolemma and the nucleus. After employing background subtraction and Gaussian blurring (sigma = 20 nm) automatic thresholding with the Triangle algorithm was performed to obtain a binarized image. Analogously Cav3 elements were extracted employing background subtraction, image smoothing, Otsu thresholding within ROIs and subsequent binary dilation to close holes. Localization of Cav1.2-clusters to Cav3-cluster positive TAT elements was defined as a complete or partial signal overlap of corresponding binary images.

Combined confocal Ca^{2+} and axial tubule imaging

For line scan imaging of AM and VM in either transversal or axial cell directions we used a LSM 710 NLO confocal microscope (Carl Zeiss; Jena, Germany) and a Plan-Apochromat 63x/1.40 oil objective. di-8-ANEPPS (40 µM, 15 min incubation prior to use; life technologies) and fluo-4 AM (10 µM, 30 min incubation; lifetechnologies) signals were recorded separately (di-8-ANEPPS: excitation 458 nm, detection 550–740 nm; fluo-4: excitation 488 nm, detection 490–540 nm) in Tyrode A (Supplemental Table 4) at room temperature. The pinhole was set at 1 airy unit (46/56 µm). For transversal scanning a 20 µm scan line (100 pixels) was used to correlate intracellular Ca^{2+} measurements with apparent membrane components as indicated (S = surface sarcolemma, AT = axial tubule, CY = off-membrane cytoplasm). The scan line was positioned randomly but excluded the nucleus. Cardiac myocytes were field-stimulated at 0.5 Hz with 3 ms voltage steps at 23 V. Images were analyzed using ImageJ (http://imagej.nih.gov/ij/). To visualize early intracellular Ca^{2+} release locations, we determined the fluo-4 fluorescence at 25% of the maximal signal amplitude (F25) and presented the F25 temporal profile. For this, the maximum signal intensity amplitude was determined for each pixel.

To correlate the latency of Ca^{2+} release for specific locations at AT and S membrane components, we analyzed the mean latency of the fluo-4 signal for distinct cytosolic regions based on the di-8-ANEPPS signal. The earliest upstroke of the Ca^{2+} transient (dF/dt) was identified by the first derivative of the fluo-4 signal 3 standard deviations above the baseline. Ca^{2+} release latency at different regions (CY, AT, S) was calculated relative to the earliest transversal fluo-4 signal initiation time.

SR Ca^{2+} load and Ca^{2+} transient measurements

Freshly isolated mouse AM and VM were plated on laminin-coated coverslips in Tyrode B (Supplemental Table 4). Cells were loaded for 20 min with 5 µM fluo-4 AM at room temperature followed by 10 min de-esterification. During measurements cells were constantly perfused with fresh Tyrode solution at room temperature. Fluo-4 was excited at 488 nm and detected >500 nm using ~1.5 ms time interval line scanning and a Plan-Apochromat 63x/1.40 oil objective (LSM 710 NLO; Carl Zeiss, Jena). Cardiac myocytes were field-stimulated at 1 Hz with 3 ms voltage pulses at 20 V. For analysis, fluorescent signals were normalized to background fluorescence obtained at rest. SR Ca^{2+} uptake rates were estimated via decay function during the diastolic phase of the Ca^{2+} transient. SR Ca^{2+} load was estimated through the amplitude of Ca^{2+} transients during 10 mM caffeine exposure in Tyrode B.

Intracellular Ca^{2+} measurements during voltage-clamp

For voltage-control of Ca^{2+} transients and Ca^{2+} sparks AM were patch-clamped using patch-clamp pipette solution (Supplemental Table 4). In addition, cells were perfused with patch-clamp extracellular solution (Supplemental Table 4). The holding potential was kept at -75 mV. Ca^{2+} sparks were recorded after five depolarizing pulses to 0 mV of 25 ms duration, after which AM were kept for 3 sec at -50 mV to record spontaneous Ca^{2+} sparks. Ca^{2+} sparks were analyzed by ImageJ (http://imagej.nih.gov/ij/) and customized routines in IDL as previously described (16). Following Ca^{2+} spark analysis, individual signal events were classified according to subcellular location (S = surface sarcolemma, AT = axial tubule, CY = off-membrane cytosol) as indicated in Figure 4.

Mathematical modeling of atrial RyR2 cluster Ca^{2+} sparks

The single sarcomere spatial model consists of two partial differential equations (PDEs): the diffusion of Ca^{2+} and Ca^{2+}-bound to indicators ([CaF], e.g., Fluo-4). These reaction-diffusion style equations are as follows,

$$\frac{\delta[Ca^{2+}]_i}{\delta t} = D_{Cai}\nabla^2[Ca^{2+}]_i + (\lambda_{dsi} J_{efflux} - J_{serca} - J_{ncx} + J_{bca} - J_{buffer} - J_{CaF})$$

$$\frac{\delta[CaF]_i}{\delta t} = D_{CaF}\nabla^2[CaF]_i + J_{CaF}$$

where λ_{dsi} is the volume fraction for the Ca^{2+} release unit (CRU) subspace to cytosol, β_i is the cytosolic dynamic buffering fraction, and the cytosolic fluxes (e.g., J_{efflux}, J_{serca}, J_{ncx}, J_{bca}, etc.) retain similar formulations to fluxes presented in Wescott *et al.* (17). These PDEs are numerically integrated using a centered difference in space and forward Euler in time solver and ordinary differential equations (ODEs) govern diadic subspace $[Ca^{2+}]_{ds}$ and junctional SR $[Ca^{2+}]_{jsr}$ (see Wescott *et al.* (17) for details). Select parameters for the modeling presented in Figures 4C and 4D and Supplemental Figure 9 are listed below.

Documentation of select modeling parameters:

kR_{12}	RyR2 opening rate	0.2 $\mu M^{-2.2}$ s^{-1}
kR_{21}	RyR2 closing rate	500 s^{-1}
kR_{12p}	Phosphorylated RyR2 opening rate	0.6 $\mu M^{-2.2}$ s^{-1}
kR_{21p}	Phosphorylated RyR2 closing rate	200 s^{-1}
D_{Cai}	$[Ca]_i$ diffusion rate	350 μm^2 s^{-1}
D_{CaF}	Fluo-4 diffusion rate	80 μm^2 s^{-1}
$[Ca^{2+}]_{nsr}$	Fixed NSR [Ca] level	1000 μM

cAMP-FRET measurements in AM

To study changes of intracellular cAMP by FRET, adult mouse AM and VM were isolated and plated on laminin-coated round glass coverslips. 1-3 h after plating, cells were washed once and maintained in Tyrode C (Supplemental Table 4) at room temperature, placed on a Zeiss Axio Observer A1 microscope equipped with a Plan-Apochromat 63x/1.4 oil immersion objective, Polychrome V light source, DV2 DualView beam splitter and a CoolSNAP-HQ2 CCD-camera (Visitron Systems, Pullheim, Germany). Cells were stimulated with 100 nM isoprenaline, and the change in YFP/CFP emission ratio upon 436 nm excitation (emission filters YFP 535 ± 15 nm, CFP 480 ± 20 nm) was monitored online at various subcellular regions and recorded by VisiView software (Visitron). After each measurement, emission values were corrected for bleedthrough of CFP into the YFP channel and for photobleaching as described (18). The data were analyzed with Excel and Origin 8.5 (OriginLab) software and presented as normalized YFP/CFP ratio in Figure 5A.

Sarcomere shortening

Freshly isolated mouse cardiomyocytes were loaded on glass coverslips in Tyrode A (Supplemental Table 4) at room temperature. Cells were quality-controlled regarding regular shape, striations and homogenous contractile behaviour as a prerequisite for regional sarcomere imaging. Myocytes which were abnormally bent, significantly deviating from the main cell axis, before or during contractions were excluded. For cell-wide contraction analysis, we used a Nikon Eclipse TE2000-U microscope in combination with an IonOptix contractility system (Milton, MA). ROIs were chosen as large as possible inside AM and at corresponding size in VM. Sarcomere shortening

was recorded during 1 Hz field stimulation with 3 ms voltage steps at 23 V. Isoproterenol and H89 were used both at a concentration of 1 µM. Contraction kinetics were analyzed by IonWizard 6.5 software (Ion Optix, Milton, MA).

Localized contraction analysis included AM from titin-eGFP knock-in mice, which allow live cell imaging of the sarcomeric M-band during contraction. ROIs of 5.6 x 6 µm including the lateral surface membrane were chosen to focus on 3 sarcomere lengths between the AM center and periphery for different time points (mean cell width: 14.4±0.3 µm). Live confocal time series of select ROIs were acquired with a Zeiss LSM 710 NLO microscope (Jena, Germany), using the Plan-Apochromat 63x/1.40 Oil objective, at a pixel size of 200 x 200 nm and a scan time of 7.09 ms per frame. eGFP was excited at 488 nm. Cells were recorded during 1 Hz field stimulation with 3 ms voltage steps at 23 V. For analysis in Fiji (http://fiji.sc/) the ROIs of 6 x 28 pixels each for sub-sarcolemmal and central ROIs from the same frames were chosen to extract the signal intensity profiles of the recorded titin-eGFP M-band signals in systole and diastole. Based on both intensity profiles sub-sarcolemmal versus central sarcomere length was calculated and analyzed each during systolic contraction and diastolic relaxation to compare local time differences and reported as relative latency difference of transversal sarcomere shortening in Figure 7C.

Protein analysis

Cardiac tissues were immediately snap-frozen and stored at -80 °C. Atrial or ventricular tissues were homogenized in ice-cold homogenization buffer (HEPES 10 mM, sucrose 300 mM, NaCl 150 mM, EGTA 1 mM, $CaCl_2$ 2 mM, Triton X-100 0.5 % (v/v), protease and phosphatase inhibitor mix (Roche), pH 7,4) using a Miccra D-1 homogenizer. The

homogenates were centrifuged at 8 g for 10 min at 4 °C to obtain the post-nuclear fraction. The supernatant was aliquoted and immediately snap-frozen. For Western blots 30 µg of protein per lane (for phosphorylation analysis 50 µg of protein) were resolved by Tris-glycine SDS-PAGE. Gradient gels (6-12 %) were cast to resolve proteins above 100 kDa (i.e. RyR2 565 kDa) and below 100 kDa (i.e. GAPDH 36 kDa) using the Mini PROTEAN 3 Cell system (BioRad). Gels were electrophoresed at constant 100 V. Proteins were transferred onto nitrocellulose membranes (0.45 µm, Protran BA 85, Whatman) using the BioRad criterion blotter (plate electrodes) at constant 100 V for a duration of 2 h in transfer buffer (Tris 32.5 mM, glycine 192 mM, 20 % (v/v) Methanol) at 4 °C. Membranes were blocked for 2 h in 5% (w/v) non-fat milk in Tris-buffered saline with 0.05% (v/v) Tween 20, and incubated with the primary antibodies documented in Supplemental Table 3 at 4 °C overnight. Blots were washed three times in blocking buffer and subsequently incubated with horseradish peroxidase-labeled anti-rabbit or anti-mouse IgG 1:10,000 in 5 % milk for a minimum period of 1 h at room temperature (GE Healthcare NA934 & NXA931). Following three washing steps with intervals of 10 min, blots were developed with chemiluminescent reagent (Immobilon Western Chemiluminescent HRP substrate, Millipore). Blots were imaged using a Kodak Imaging Station 4000R system. Band densitometry analysis was performed using Carestream MI Software V.5.0.3 and normalized to GAPDH. PKA phosphorylation changes were normalized to control.

Transaortic constriction (pTAC) and *in vivo* phenotyping

To induce aortic pressure overload, a minimally invasive transverse aortic constriction (TAC) procedure was performed on 11 weeks old male C57BL/6N mice as previously

described (19). Mice were anesthetized with 1.5–2 % isoflurane in oxygen using a rodent ventilator (Harvard Apparatus). Constriction of the transverse aorta was induced using a 27 G spacer and a 5-0 polyviolene suture. Sham operated animals underwent the same surgical procedure but without aortic constriction. For analgesia buprenorphine (0.12 µg per g body weight) was injected subcutaneously prior to surgery, and metamizole (1.33 mg/ml) treatment occurred via drinking water starting 2 days before surgery and until 7 days after the TAC operation. Doppler velocity measurements using a 20 MHz probe were conducted to estimate the post-TAC pressure gradient by transthoracic echocardiography (Vevo 2100, VisualSonics).

For in vivo cardiac phenotyping 4 weeks after TAC intervention, we performed transthoracic echocardiography of the left ventricle as described previously (11). To induce anesthesia prior to echocardiography we used 2.5% isoflurane, which was maintained at 1.5% in oxygen. Using a 30 MHz transducer left parasternal long- and short-axis views were digitally recorded. Body temperature, respiration rate and the surface electrocardiogram (ECG) were monitored throughout surgical and echocardiography procedures. To avoid errors arising from bias, the investigators were blinded for treatment and genotype.

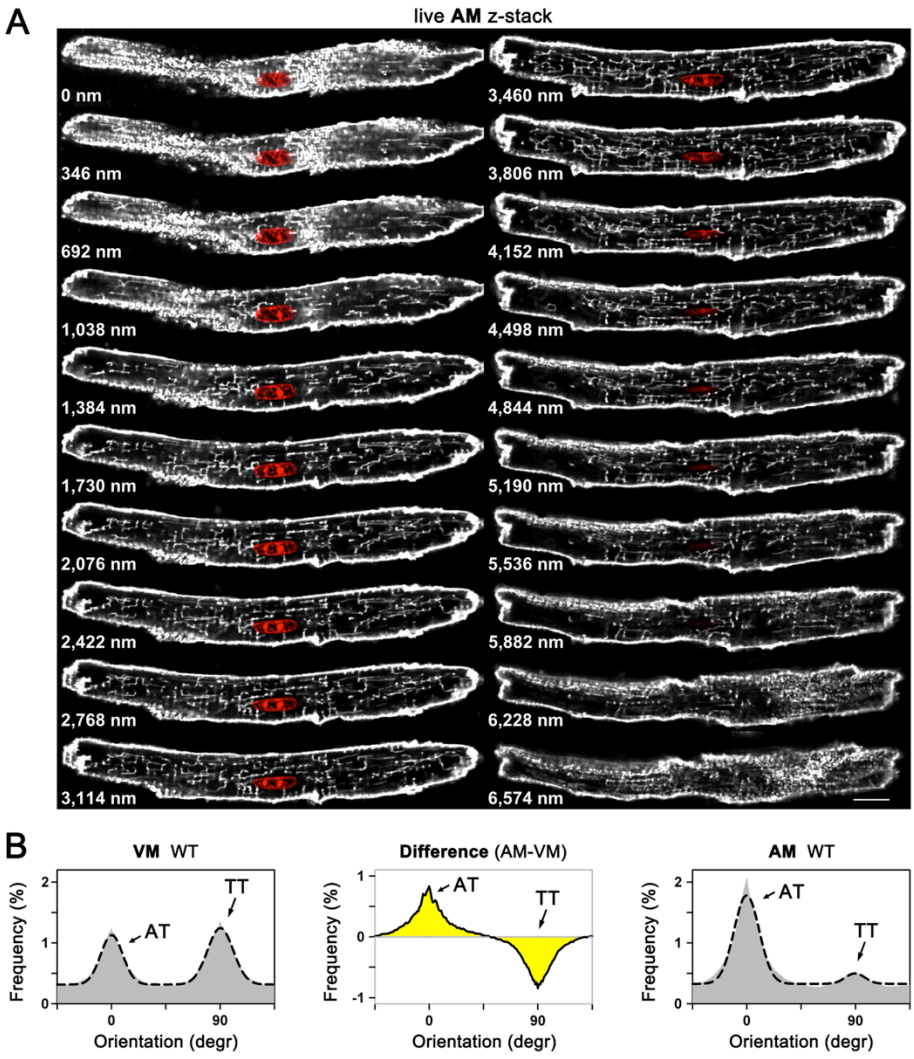

Supplemental Figure 1. Analysis of transverse-axial tubule (TAT) network components and differences between ventricular (VM) and atrial myocytes (AM). (**A**) Z-stack images show confocal live cell visualization of intracellular TAT membrane structures stained with di-8-ANEPPS. AM were adhered to a laminin coated glass coverslip and imaged from the bottom to the top using a step size of 346 nm as indicated on the lower left corner of each image. The nucleus stained by Hoechst (20 µg/ml) is colored red. Scale bar: 10 µm. (**B**) Comparison of cell-specific ventricular versus atrial TAT network components in VM and AM. *Left*: Orientation analysis of TAT components in VM highlighting transversal tubules (90°/TT) as the major peak and axial tubules (0°/AT) as the minor peak. *Center*: Subtraction (AM–VM) of the histogram integrals highlights differences between the cell-specific TAT component orientations in AM and VM. *Right*: for comparison the same AM data of Figure 1A are shown. Cell numbers: AM 36, VM 25.

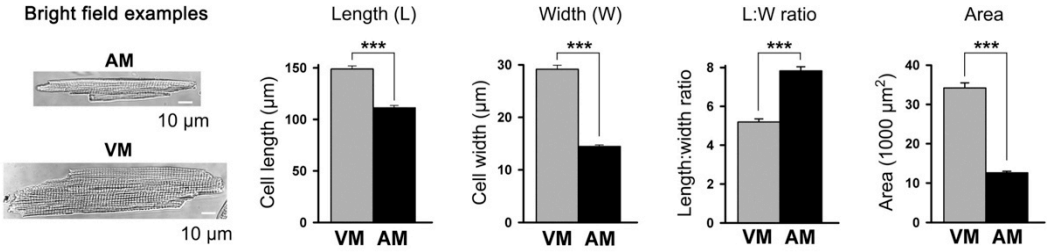

Supplemental Figure 2. The morphology and dimensions of AM versus VM from adult mouse hearts are compared. *Left*: Representative bright field images of AM and VM cells showing intact membrane boundaries and sarcomere striations. Note distinct cell-specific morphologies. Bar graphs comparing characteristic cell dimensions of VM versus AM. Measurements include cell length, cell width, length:width ratio, and area size. Cell numbers from the same wild-type hearts representative of AM 39, VM 28. Student's t-test: ****P*<0.001.

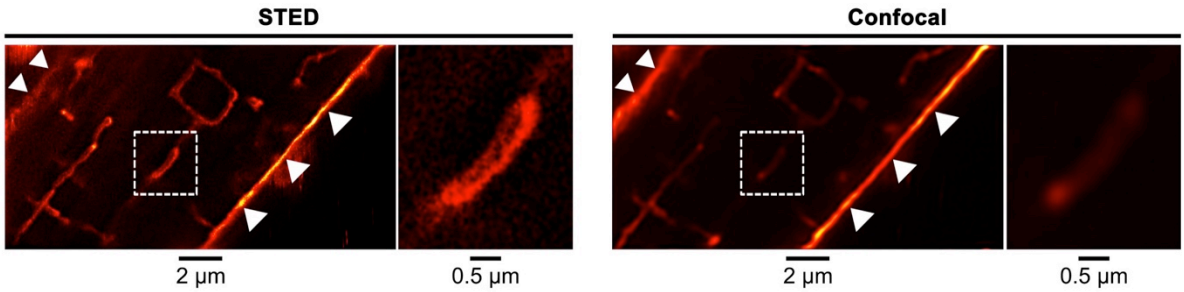

Supplemental Figure 3: Live cell superresolution STED versus confocal microscopy of TAT membrane structures in AM. STED was used to resolve nanometric details of intracellular membrane tubules in AM cells. *Left*: STED image and mangnified ROI as indicated. *Right*: Corresponding confocal image and mangnified ROI as indicated. The dashed boxes show the positions of corresponding axial tubule (AT) magnifications. Note: while the same optical light path was used both for confocal and STED imaging, the confocal images show a blurred and generally shallow signal pattern of the AT membrane tubule with insufficient signal contrast for local analysis of AT width; STED showed clearly contrasted AT components allowing for local width measurements. Triangles mark the extracellular side of the lateral surface membrane on either AM cell side for orientation.

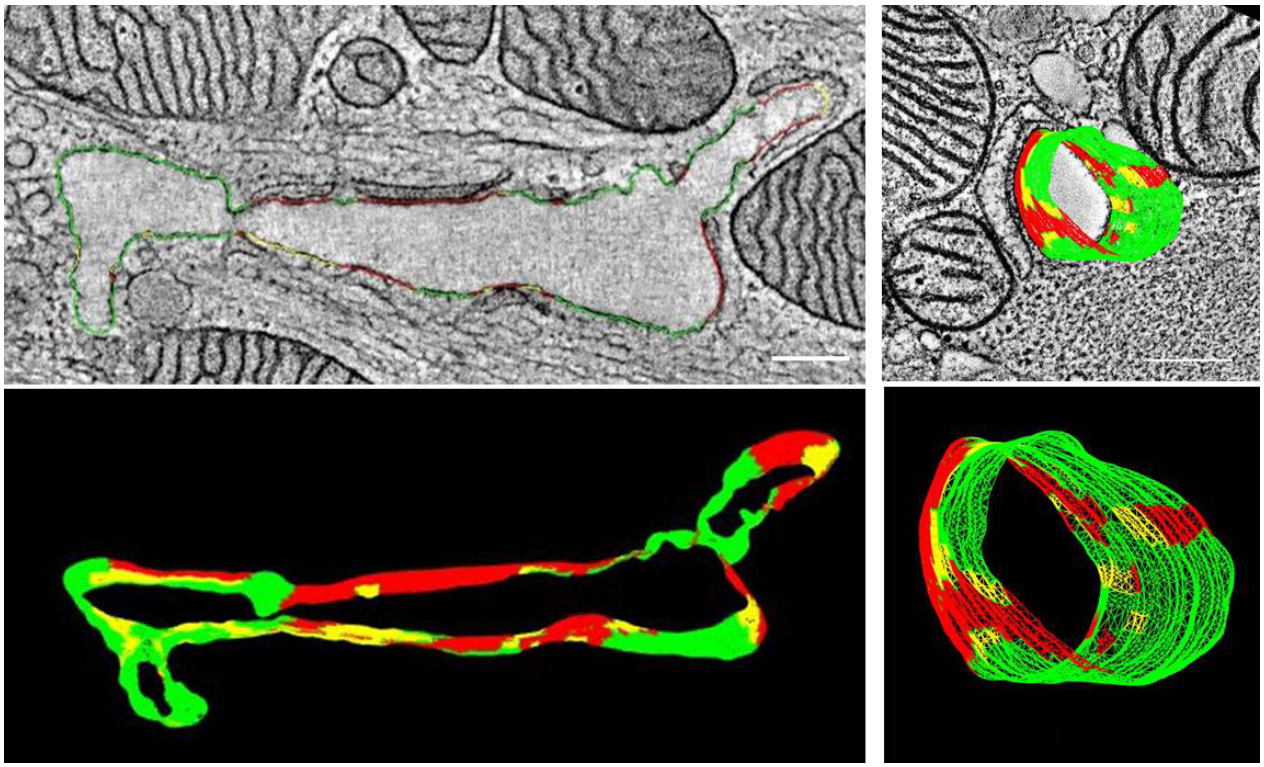

Supplemental Figure 4: 3D rendering of electron tomography (ET) data (top) and final 3D model (bottom) of the images shown in Figure 1D. Top row, left panel shows a representative axial tubule (AT) cut in a longitudinal direction. Top row, right panel shows representative AT cut at a cross-section (note: AT not the same as left panel). Bottom row, illustrates 3D renderings of AT from the ET data stack, with color-coding indicative of the association with juxtapositioned sarcoplasmatic reticulum (SR) membranes: red - AT–SR junctions ≤15nm in gap width containing RyR2 densities, yellow - AT–SR junctions ≤20nm in gap width but lacking RyR2 densities, and green - membrane areas with no apparent junctions. Scale bars: 200 nm.

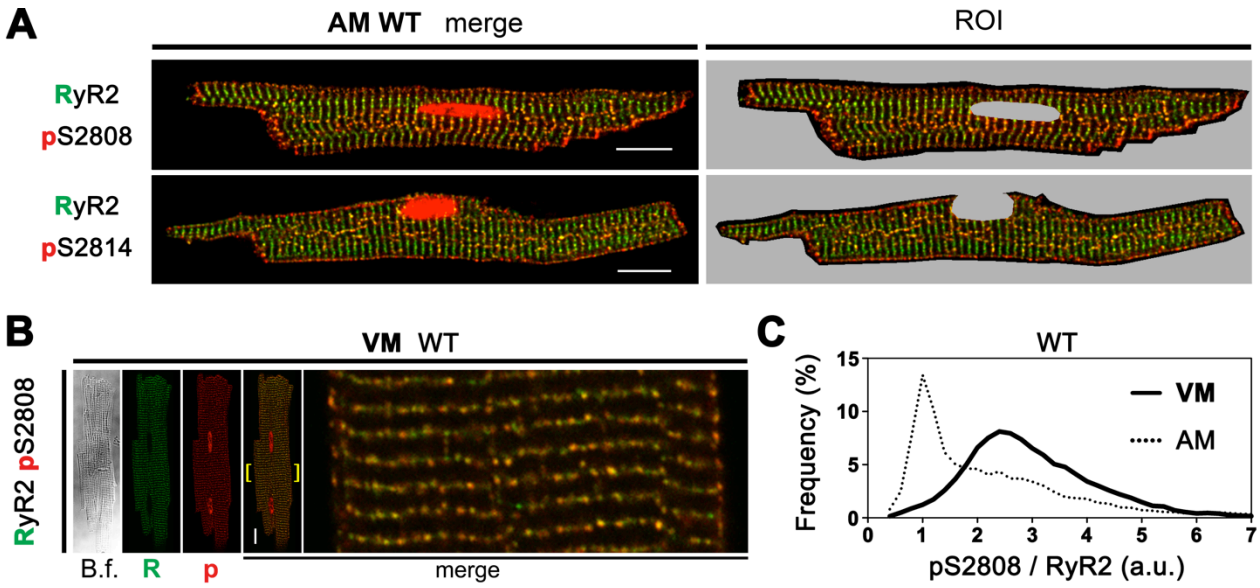

Supplemental Figure 5. Immunofluorescence image analysis, and RyR2-pS2808 cluster and frequency distribution in ventricular myocytes (VM). (**A**) *Left*: RyR2 and RyR2-pS2808 or RyR2-pS2814 immunostained AM are compared to visualize principally similar highphos cluster patterns in strings-of-pearls. *Right*: For quantitative highphos cluster analysis, the region of interest (ROI) was chosen to exclude the nucleus due to unspecific antibody cross-reaction (corresponding with Figure 3A/D and Supplemental Table 3). Scales: 10 µm. (**B**) VM immunostained with the same RyR2 and RyR2-pS2808 antibodies show overall homogenously distributed RyR2 cluster signals. B.f., bright field; scale: 10 µm. (**C**) The pS2808/RyR2 frequency distribution from VM cells shows a Gaussian distribution, which is significantly different from the AM distribution presented in Figure 3B (dotted line). Different cell types are indicated by legend.

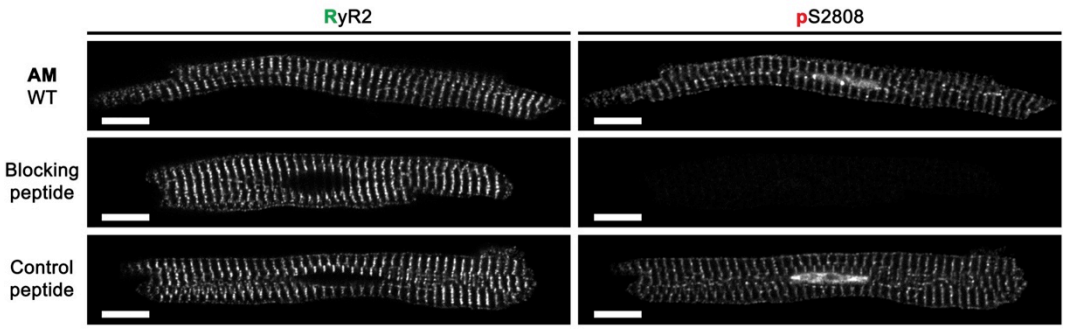

Supplemental Figure 6. Imaging studies using recombinant peptides. Distinct recombinant peptides were used to confirm the phospho-epitope specific RyR2-S2808 in situ labeling in PKA phosphorylation-competent wild-type (WT) AM. *Top row*: in AM control cells, the primary RyR2 and RyR2-pS2808 antibody labeling was applied as described for the co-immunostaining standard protocol above. *Middle row*: the blocking peptide was incubated with primary antibodies 20 min prior to staining. The blocking peptide RyR2-2802_2813 mimics the phosphorylated RyR2-S2808 residue based on the sequence H_2N-CRT RRI S(PO_3H_2)QT SQV-$CONH_2$. *Bottom row*: the control peptide mimics the de-phosphorylated RyR2-S2808 residue and was incubated with primary antibodies 20 min prior to staining. Scale bars, 10 μm.

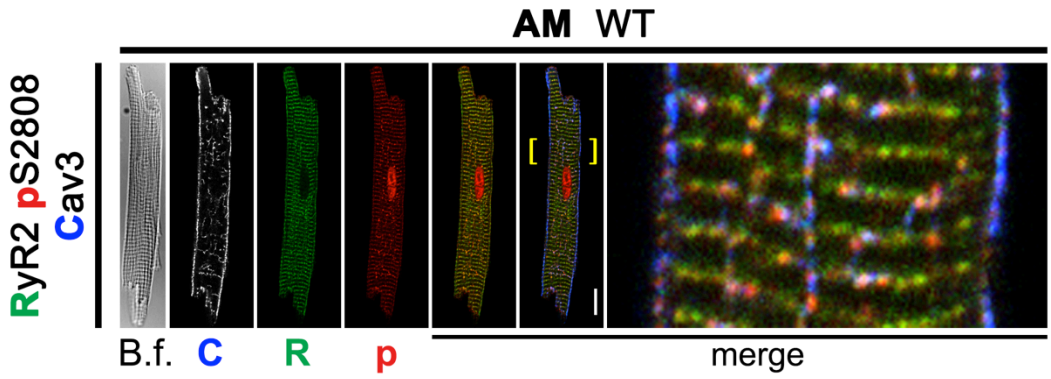

Supplemental Figure 7. Triple staining of AM. AM were labeled with Cav3, RyR2 and RyR2-pS2808 primary antibodies. Highphos RyR2 clusters (yellow) are aligned in central-axial structures alternating with Cav3 clusters (blue). Lowphos RyR2 clusters (green) are not associated with Cav3-labeled structures. B.f.: bright field; scale: 10 µm.

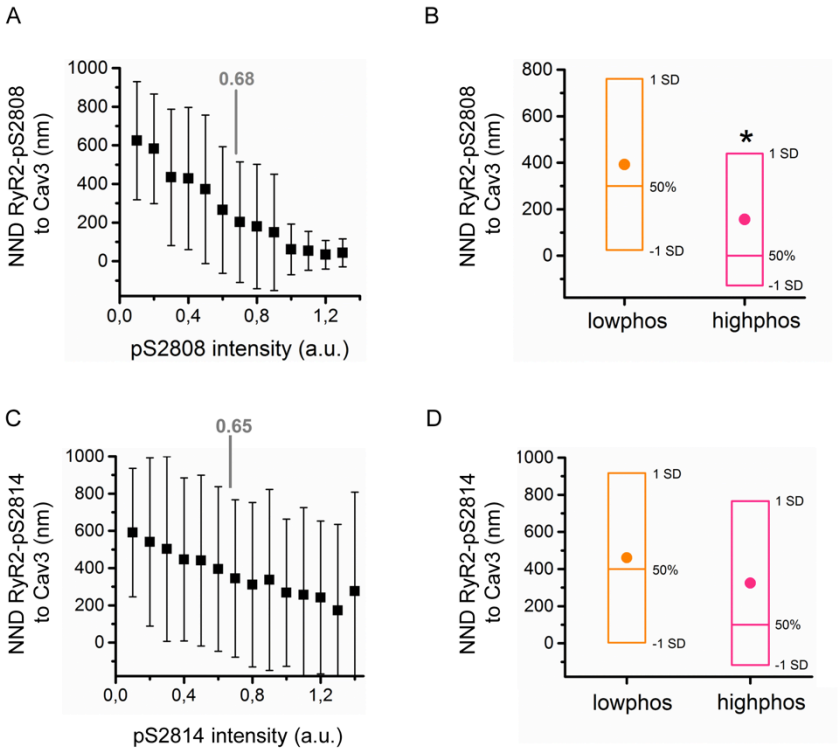

Supplemental Figure 8. Proximity analysis of highphos RyR2-clusters relative to TAT membrane structures. Image analysis comparing the spatial association of Cav3-labeled TAT structures and highphos RyR2-clusters for (**A, B**) Ser-2808 phosphorylated by PKA and (**C, D**) Ser-2814 phosphorylated by CaMK. Nearest-neighbor-distance (NND) to Cav3-clusters versus phosphorylation signal intensity of (**A**) RyR2-pS2808- and (**C**) RyR2-pS2814-clusters were inversely correlated (Pearson R -0.38 and -0.18, respectively). Threshold for highphos cluster detection indicated on top. n cells/RyR2-clusters: pS2808/pS2814 data from 7/20 AM encompassing 1988/5922 individual RyR2-clusters, respectively. (**B, D**) RyR2-clusters grouped into highphos and lowphos clusters using the average signal intensity as threshold. pS2808/pS2814 represent 997/3153 lowphos clusters (orange) and 991/2769 highphos clusters (magenta). The NND spacing between RyR2-pS2808 and Cav3 is significantly smaller for highphos clusters. Mann-Whitney test: * $P<0.05$. Moreover, highphos RyR2-clusters directly co-localize or overlap with Cav3-clusters more frequently than lowphos RyR2-clusters.

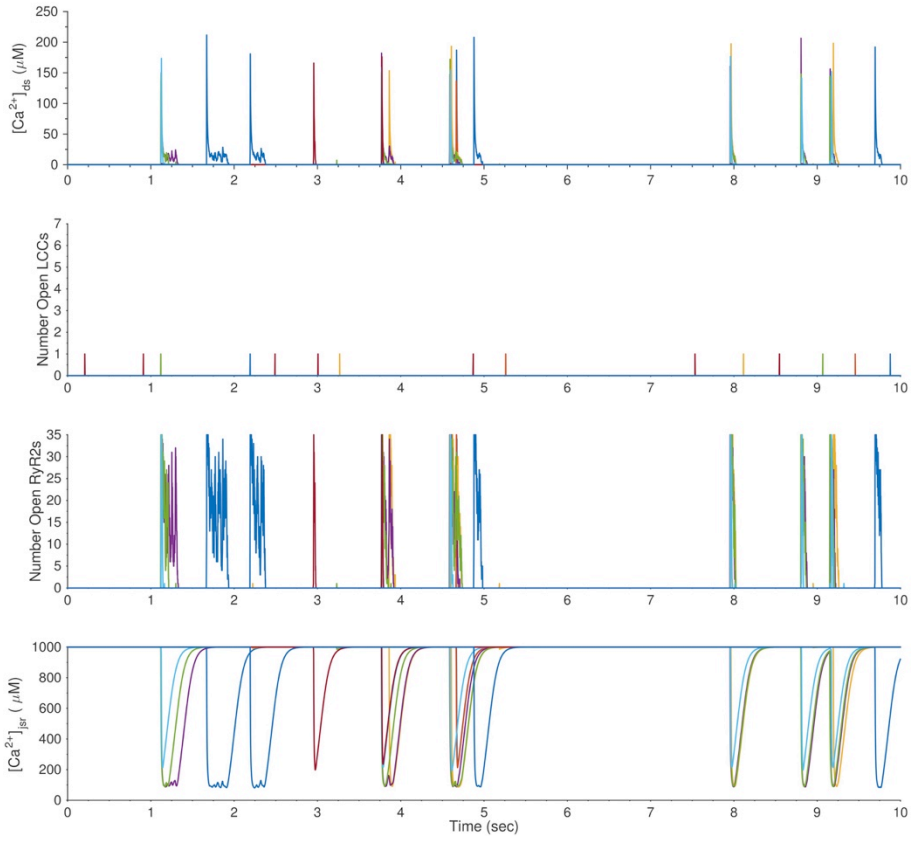

Supplemental Figure 9. Mathematical modeling of atrial Ca^{2+} sparks and blinks. From top to bottom: average $[Ca^{2+}]_{ds}$ in the dyadic subspace of the CRU, number of open LCC (Cav1.2) channels, number of open RyR2 channels, and average junctional SR $[Ca^{2+}]_{jsr}$ load during stochastic Ca^{2+} spark events with modeling initiated at t = 0 ms. Panels show traces for single representative sparks; averages were calculated from at least 100 sparks. For details about the mathematical modeling approaches please refer to Wescott *et al.* (17).

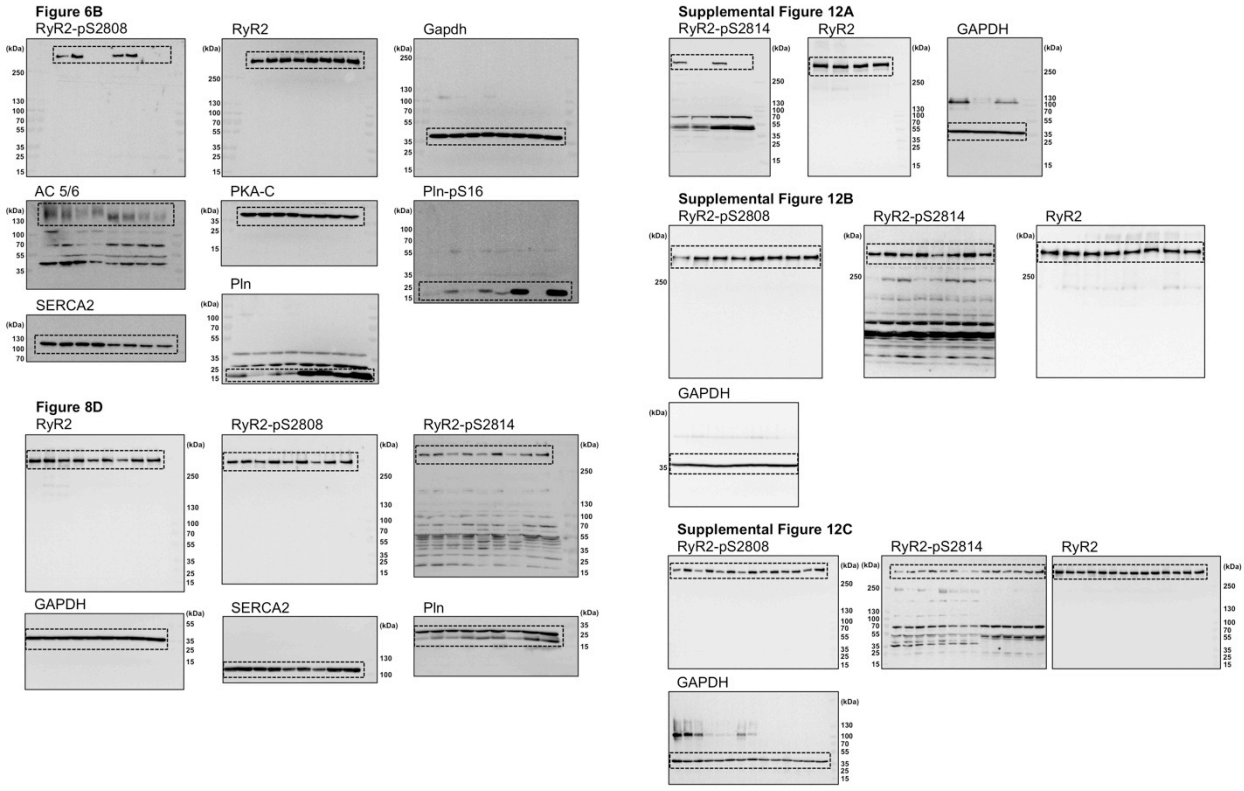

Supplemental Figure 10. Full scans of Western blots reported. Dashed frames indicate the data presented in the manuscript Figures.

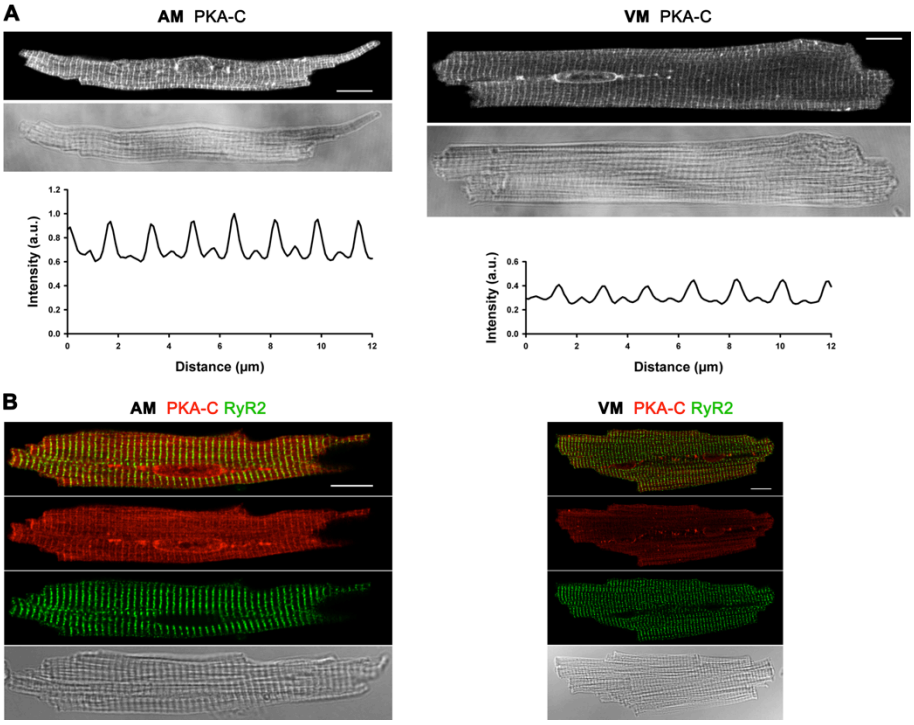

Supplemental Figure 11. Confocal immunofluorescence images of PKA catalytic subunit (PKA-C) striations in AM and VM from the same wild-type mouse hearts. (**A**) *Left:* AM image of PKA-C and corresponding bright field view revealing protein expression at sarcomeric Z-bands (major signal) and M-bands (minor signal), and corresponding signal intensity profile. *Right*: VM image of PKA-C signal pattern showing generally thinner striations at the Z-bands compared to AM, and corresponding bright field view and signal intensity profile. Note: the increased signal intensity amplitude of PKA-C striations in AM correlates with significantly higher PKA-C protein expression in AM compared to VM. Scale bars: 10 μm. (**B**) Confocal co-localization image study of AM versus VM labeled for PKA-C and RyR2. Green and red channels are indicated on top; yellow signals indicate a high degree of local co-localization; bottom, corresponding bright field images. Scale bars, 10 μm.

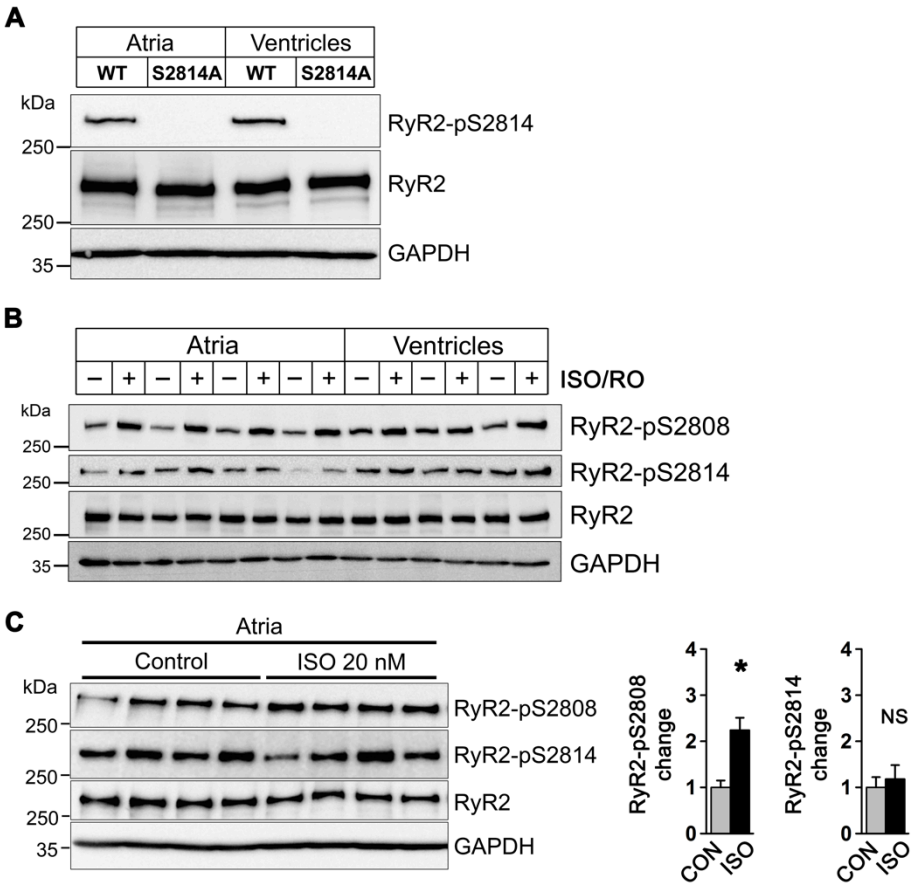

Supplemental Figure 12. (**A**) Immunoblots comparing atrial and ventricular tissue from WT and CaMK phosphorylation-incompetent RyR2-S2814A$^{+/+}$ (S2814A) mouse hearts as indicated. These experiments confirmed specific detection of the pS2814 epitope. (**B**) Immunoblots comparing untreated (-) control versus maximal ISO/RO (1 μM/10 μM) treated (+) atrial and ventricular tissue lysates for PKA phosphorylation at the RyR2-S2808 and CaMK phosphorylation at the RyR2-S2814 site. Accordingly, Figure 6C shows the corresponding RyR2-pS2814 data normalized to the RyR2 substrate. (**C**) Immunoblots from atrial tissue lysates from mouse hearts, stimulated with a low nanomolar ISO concentration (20 nM) for 2 min, and immunoblotted for RyR2-S2808 and RyR2-S2814 phosphorylation. In contrast to the pS2814 change, the pS2808 change normalized to RyR2 was more than 2-fold increased after 20 nm ISO stimulation.

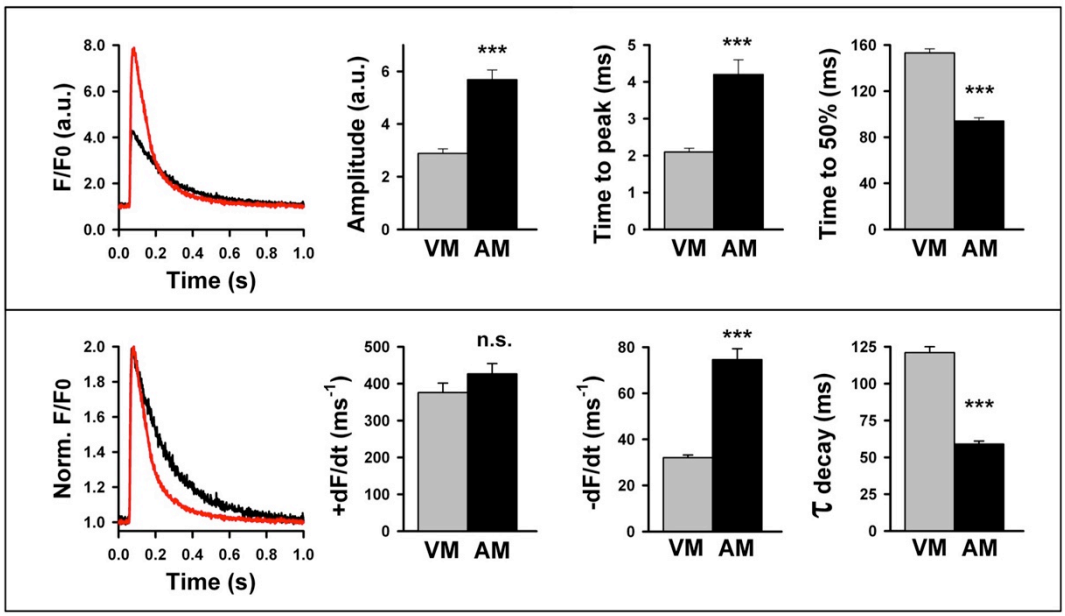

Supplemental Figure 13. Ca^{2+} transient measurements in intact AM and VM. Comparison of intracellular Ca^{2+} transient measurements in AM versus VM cells. *Left*: Representative traces during pacing show steady-state intracellular Ca^{2+} transients confocally imaged in AM (red) and VM (black). AM traces (red) show a significantly larger amplitude (*top*) and significantly faster decay (*bottom*) compared to VM (black) from the same WT mouse hearts. *Bar graphs*: comparison of physiologically important Ca^{2+} transient parameters of VM and AM. Cell numbers isolated from the same WT hearts: AM 36, VM 47. Student's t-test: ****P*<0.001; n.s., not significant.

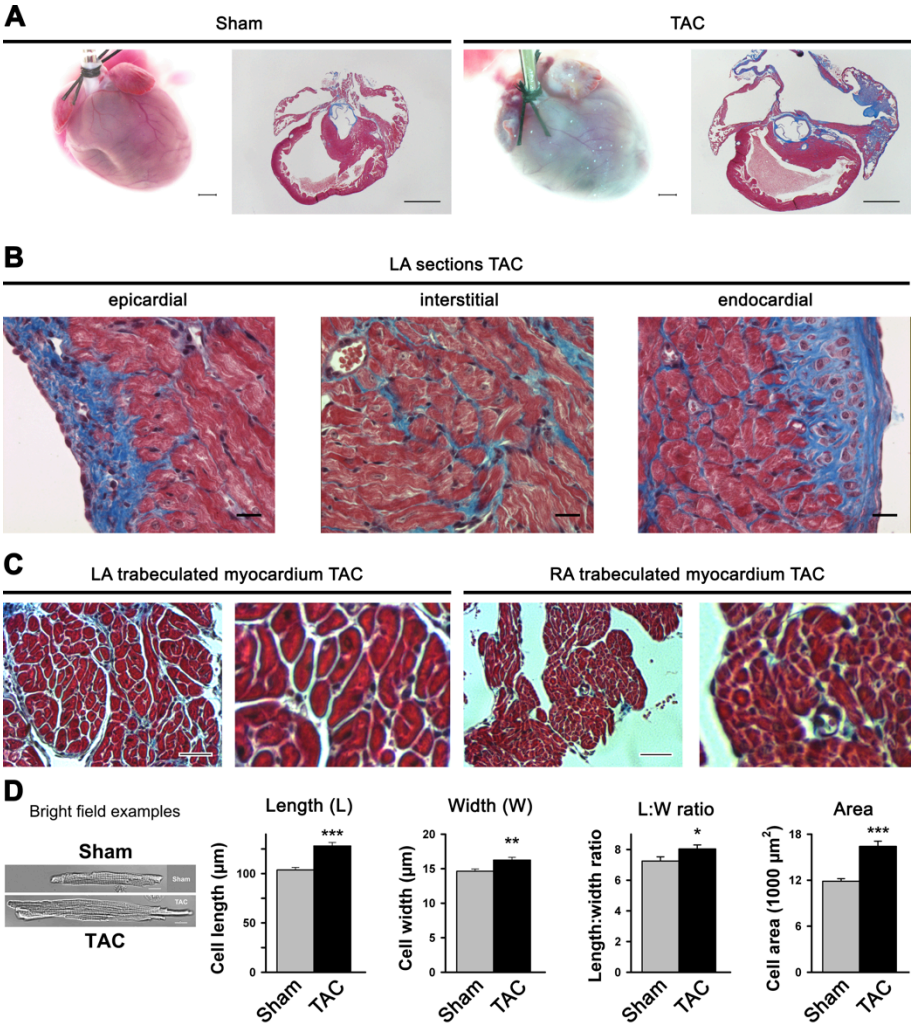

Supplemental Figure 14. Histomorphological changes and AM dimensions 4 weeks post-TAC. (**A**) Langendorff-perfused hearts and Masson-Trichrom stained sections (LA, RA, RV) at the aortic root comparing sham and post-TAC hearts. Note the profound LA dilation and select fibrosis of the LA but not RA chamber post-TAC. Scales: 0.7 mm. (**B**) LA sections from the same post-TAC heart showing profound epicardial and endocardial fibrosis and moderate interstitial fibrosis. Scales, 20 µm; Masson-Trichrom stain. (**C**) LA versus RA post-TAC trabeculated myocardial sections (*left*) and magnifications (*right*). Note the hypertrophied AM cross-sections in the LA but not the RA myocardial sections. Scales, 20 µm; Masson-Trichrom stain. (**D**) Left AM from post-TAC hearts developed a significantly increased cell size as compared to AM from sham hearts. *Left*: Bright field views of isolated left AM from sham versus post-TAC hearts as example of significant hypertrophy post-TAC. *Right*: Bar graphs comparing AM cell dimensions of sham and post-TAC hearts. AM cell numbers: sham 34, pTAC 41. Scale bars: 10 µm. Student's t-test: **P*<0.05; ***P*<0.01; ****P*<0.001.

Supplemental Table 1

AT and TT dimensions in intact TAT networks (STED nanoscopy data)

	VM	AM	*P* value
Central Axial Tubule (AT)	n = 27	n = 30	
Width (nm)	200.7 ± 8.5	293.3 ± 7.7	< 0.001
Circumference (nm)	630.6 ± 26.7	921.5 ± 24.3	< 0.001
Surface area ($\mu m^2/\mu m$)	0.631 ± 0.03	0.922 ± 0.02	< 0.001
Central Transverse Tubule (TT)	n = 117	n = 48	
Width (nm)	193.9 ± 3.0	240.19 ± 8.4	< 0.001
Circumference (nm)	609.4 ± 9.6	754.58 ± 26.6	< 0.001
Surface area ($\mu m^2/\mu m$)	0.609 ± 0.01	0.755 ± 0.027	< 0.001
Surface Transverse Tubule (TT)	n = 224	n = 76	
Width (nm)	191.4 ± 2.4	242.0 ± 7.7	< 0.001
Circumference (nm)	601.4 ± 7.7	760.3 ± 24.4	< 0.001
Surface area ($\mu m^2/\mu m$)	0.601 ± 0.08	0.760 ± 0.02	< 0.001

AM, atrial myocyte; VM, ventricular myocyte. *P* values, Student's t-test.
Figure 1C shows a cartoon corresponding with the depicted AT dimensions.
Whereas AT width was measured by STED microscopy, here AT circumference and surface area were mathematically calculated.

Supplemental Table 2

Cardiac in vivo phenotyping 4 weeks after transaortic constriction (post-TAC)

	Sham	post-TAC	*P* value	Significance
Heart weight				
Count (n)	17	24		
Age (weeks)	15	15		
Body weight (g)	26.2 ± 0.4	25.2 ± 0.4	0.093	NS
Heart weight (mg)	238.4 ± 6.9	380.1 ± 12.3	< 0.001	***
HW/BW (mg/g)	9.1 ± 0.3	15.1 ± 0.5	< 0.001	***
Doppler echocardiography				
Count (n)	28	30		
Aortic gradient (mmHg)	3.54 ± 0.2	77.9 ± 1.9	< 0.001	***
LA echocardiography				
Count (n)	19	21		
LA ID, diastole (mm)	2.15 ± 0.07	2.80 ± 0.12	< 0.001	***
LA ID, systole (mm)	1.79 ± 0.06	2.44 ± 0.14	< 0.001	***
LA FS (%)	18.16 ± 1.48	11.66 ± 1.41	0.004	**
LV echocardiography				
Count (n)	28	30		
Heart rate (min^{-1})	456.5 ± 9.5	487.5 ± 11.4	0.043	*
LV AWTh, diastole (mm)	0.77 ± 0.01	1.14 ± 0.02	< 0.001	***
LV ID.d, diastole (mm)	4.40 ± 0.05	4.59 ± 0.06	0.026	*
LV ID.s, systole (mm)	3.55 ± 0.07	3.81 ± 0.09	0.023	*
LV FS (%)	19.1 ± 1.2	16.7 ± 1.2	0.159	NS
LV FAS (%)	35.0 ± 1.1	27.1 ± 1.7	< 0.001	***

Legend: LA, left atrium; LV, left ventricle; ID, inner diameter; FS, fractional shortening; AWTh, anterior wall thickness in diastole; FAS, fractional area shortening; Student's t-test: *P<0.05; **P<0.01; ***P<0.001; NS, not significant.

Supplemental Table 3

Documentation of primary antibodies used for immunofluorescence imaging (IF) and Western blotting (WB)

Protein of interest	Species	Clonality	Clone	Antigen / Immunogen	Company	Catalog no.	Concentration	Dil. (WB)	Dil. (IF)	IF cross reaction
A cyclase V/VI	rabbit	polyclonal		peptide mapping at the C-terminus of A cyclase V of human origin	Santa Cruz Biotechnology, inc.	sc-590	200 µg/ml	1:250		
Cav1.2	rabbit	polyclonal		peptide (C)TTKINMDDLQPSENEDKS, corresponding to amino acid residues 848-865 of rat Cav1.2	Alomone labs	ACC-003	0.8 mg/ml		1:500	yes (nucleus)
Caveolin 3	mouse	monoclonal	26/Caveolin3	rat caveolin 3 aa. 3-24	BD Biosciences	610421	250 µg/ml		1:500	no
Caveolin 3	rabbit	polyclonal		aa. 1-18 of rat caveolin 3	Abcam	ab2912	1 mg/ml		1:500	no
Gapdh	mouse	monoclonal	6C5		Biotrend	5G4 Mab 6C5	5.3mg/ml	1:160,000		
Phospholamban	mouse	monoclonal	2D12	synthetic peptide corresponding to Dog Phospholamban aa 2-25.	Abcam	ab 2865		1:12500		
Phospholamban phosphoSerin16	rabbit	polyclonal		phosphopeptide comprising residues 9-19-Y (residues R9SAIRRAS(PO3H2)TIE19Y) conjugated to KLH	Badrilla Ltd.	A010-12	20µg/100µl	1:1000		
PKA catalytic subunit	rabbit	polyclonal		epitope mapping at the C-terminus of PKAα cat of human origin	Santa Cruz Biotechnology, inc.	sc-903	200µg/ml	1:500	1:100	no
Ryanodine Receptor 2	mouse	monoclonal	C3-33	canine cardiac RyR	Thermo Scientific	MA3-916	1 mg/ml		1:500	no
Ryanodine Receptor 2	rabbit	polyclonal		aa. QDEVRGDGEEGERKPLEAALPSEDLTDLKELTE ESDLLSDIFGLDLKREGGQYKLIPHNPNAGLSDLMS NPVPMPEVQEKFQEQKAKEEEKEEKEETKSEPE	Sigma-Aldrich	HPA 020028	0.18mg/ml	1:2500		
Ryanodine Receptor 2 phosphoSerin2808	rabbit	polyclonal		synthetic peptide (YNRTRRIS(PO3H2)QT2810) conjugated to keyhole limpet haemocyanin	Badrilla Ltd.	A010-30		1:1000	1:500	yes (nucleus)
Ryanodine Receptor 2 phosphoSerin2814	rabbit	polyclonal		synthetic peptide corresponding to aa. surrounding the phosphorylated serine residue at position 2814 of RyR2(human) conjugated to KLH	Badrilla Ltd.	A010-31		1:500		
Ryanodine Receptor 2 phosphoSerin2814	rabbit	polyclonal			custom-made		0.2mg/ml		1:250	yes (nucleus)
Serca2a	rabbit	polyclonal		synthetic peptide (C-LEPAILE997) corresponding to aa. at the extreme C-terminus of SERCA2a	Badrilla Ltd.	A010-20		1:1000		

Supplemental Table 4

Composition of physiological buffer solutions used during cell isolation, patch-clamp electrophysiology, and live cell imaging as referenced in the methods section.

Patch-clamp extracellular solution	NaCl 140 mM, CsCl 5 mM, $MgCl_2$ 1.2 mM, $CaCl_2$ 1 mM, HEPES 10 mM, Na_2HPO_4 0.33 mM, Glucose 10 mM, pH 7.4 (NaOH)
Patch-clamp pipette solution	CsAsp 70 mM, TEA-Cl 10 mM, CsCl 55 mM, Na_2ATP 5 mM, HEPES 10 mM, EGTA 1 mM, $CaCl_2$ 0.219 mM (for 50 nM free $[Ca^{2+}]$), K_5Fluo-3 100 µM, pH 7.2 (CsOH)
Perfusion buffer	NaCl 120.4 mM, KCl 14.7 mM, KH_2PO_4 0.6 mM, Na_2HPO_4 0.6 mM, $MgSO_4$ 1.2 mM, HEPES 10 mM, $NaHCO_3$ 4.6 mM, taurine 30 mM, 2,3-butanedione-monoxime 10 mM, glucose 5.5 mM, pH 7.4 (NaOH)
Tyrode A	NaCl 140 mM, KCl 5.4 mM, $MgCl_2$ 1.2 mM, HEPES 10 mM, Na_2HPO_4 0.33 mM, $CaCl_2$ 1 mM, glucose 10 mM, pH 7.4 (NaOH)
Tyrode B	NaCl 140 mM, KCl 5.4 mM, $MgCl_2$ 1.2 mM, HEPES 10 mM, Na_2HPO_4 0.33 mM, $CaCl_2$ 1.2 mM, glucose 10 mM, pH 7.4 (NaOH)
Tyrode C	NaCl 144 mM, KCl 5.4 mM, $CaCl_2$ 1 mM, $MgCl_2$ 1 mM, HEPES 20 mM, pH 7.4 (NaOH)